Unsteady secondary motion of pulsatile turbulent flow through a double 90°-bend duct

Junichi Oki[1] (ORCID: 0000-0002-3973-4154), Yukika Kuga[1], Ryo Yamamoto[2], Kazuhiro Nakamura[2], Hideaki Yokohata[2], Keiya Nishida[1], Yoichi Ogata[1] (ORCID: 0000-0002-9372-4299)

[1]*Department of Mechanical Systems Engineering, Hiroshima University, 1-4-1 Kagamiyama, Higashihiroshima, Hiroshima 739-8527, Japan*

[2]*Mazda Motor Corporation, 3-1 Shinchi, Fuchu-cho, Aki-gun, Hiroshima 730-8670, Japan*

Corresponding author: Yoichi Ogata

E-mail: yogata@hiroshima-u.ac.jp

Telephone: +81-82-424-7555

Abstract

We investigate turbulent flow with highly pulsating axial velocity passing through a duct with both first and second bends. The time-dependent velocity fields downstream of the bends were measured using time-resolved stereo particle image velocimetry for the steady case (Reynolds number $Re = 36,700$) and the pulsatile case ($Re = 37,800$ and Womersley number $\alpha = 59.1$). Proper orthogonal decomposition (POD) of the in-plane velocity data isolates the energetic structures of the secondary flow. The modes downstream of the first bend have a Dean motion (mode 0), single swirl (mode 1), and double swirl (mode 2), which agree with those of previous studies on steady turbulent flow. Downstream of the second bend, additional vortices appear in the modes owing to the secondary flow originating in the first bend. The modal structure of the pulsatile case is virtually the same as that of the steady case. To our knowledge, we are the first to find swirl switching in pulsatile flow, whereas the switching has been reported only for steady cases. We further conduct a time-frequency analysis via wavelet transformation onto the POD time coefficient, showing intermittency in energy of the mode associated with swirl switching.

Keywords

Turbulence, Pulsatile flow, Secondary flow, Particle image velocimetry, Swirl switching

1 Introduction

Flow in internal combustion engines is three-dimensional and highly unsteady and has been widely studied. Many studies have focused on in-cylinder flow and some on flow inside intake and exhaust manifolds, which we address in this study. Recently, Merati et al. [1] measured the flow fields upstream of a catalytic converter using stereo particle image velocimetry (PIV) to achieve optimal conversion efficiency. Xu [2] numerically simulated flow uniformity and pressure loss in an intake manifold because both factors impact engine performance. Many studies on intake/exhaust flow have used realistic manifold geometries where the flow field is highly complicated, and little has been reported on more detailed flow dynamics (such as curvature-related secondary flow) in a simple component in engine manifolds. This study focuses on unsteady flow passing through only a curved section, which is essential in engine manifolds, and is based on previous findings on bend flows.

The pioneering work on bend flow is by Dean [3, 4], who first derived the equation for laminar flow through a circular curved pipe. He theoretically found secondary motion in the pipe cross section consisting of two counter-rotating vortices [3], known as Dean vortices.

Roughly half a century after Dean's work, Lyne [5] theoretically found two additional vortices, circulating in the opposite direction to the Dean vortices, for oscillatory laminar flow (which has a zero-mean oscillating flow rate) through a circular curved pipe. This secondary motion is now called the Lyne vortices.

Subsequently, many researchers have found secondary motion of unsteady flow by studying physiological problems. Chang and Tarbell [6] found secondary vortices similar to the Lyne vortices under physiological pulsation (pulsation with non-zero-mean flow). Sudo et al. [7] classified secondary flows into five patterns; Dean, deformed Dean, intermediate between Dean and Lyne, deformed Lyne, and Lyne, for oscillatory laminar flow. More recent studies on physiological pulsatile flows [8, 9] have identified multiple vortices as well as the Dean and Lyne types. Most studies that combine secondary flow features and unsteady conditions, including the aforementioned studies on unsteady bend flows, have been restricted to low Reynolds number (laminar flow), which is far from engine conditions.

For turbulent bend flow (without pulsation), an important finding was by Tunstall and Harvey [10], who experimented with turbulent flow through an L-shaped 90°-bend pipe. They observed that secondary flow downstream of the bend was dominated by an alternating clockwise/anticlockwise single swirl instead of the classical Dean vortices. They also suggested that this abrupt switching was associated with the flow separation along the inner wall of the bend. Brücker [11] further studied unsteady secondary motion via PIV and found that the symmetry plane of the Dean vortices oscillated about the symmetry plane of the bend pipe.

Brücker [11] used the term "swirl-switching" in citing the result of Tunstall and Harvey [10]. This term is now widely used to refer to unsteady behavior of secondary vortices. Twenty-first century advances in computational resources and experimental techniques have encouraged further study of swirl switching. Rütten et al. [12] performed large-eddy simulations (LESs) of turbulent

flow in a 90° bend at Reynolds number $Re = 5,000 - 27,000$ ($Re = w_b D/\nu$, where w_b is the bulk velocity, D is the pipe diameter, and ν is the kinematic viscosity). They showed that switching can occur when there is no separation, contrary to the claim by Tunstall and Harvey [10], and found that the overall force onto the pipe wall, which causes pipe fatigue, oscillates at a low frequency corresponding to a Strouhal number $St \approx 0.01$ ($St = fD/w_b$, where f is the frequency). This oscillating force is due to the fact that one of the cells of the Dean vortices is alternately suppressed by the other cell, which is the swirl switching.

Proper orthogonal decomposition (POD) has been widely used to investigate swirl switching since the work of Sakakibara et al. [13], who applied it to velocity fields obtained from stereo PIV conducted on pipe cross sections downstream of a 90° bend at $Re = 120,000$. The result was that the velocity field reconstructed by the first POD mode with the mean field was similar to swirl switching. Spectral analysis of the time-dependent POD coefficient revealed a peak at $St = 0.07$. In a similar analysis, where Hellström et al. [14] performed stereo PIV and POD for $Re = 25,000$, the first POD mode represented a single swirl pattern, and the spectrum of the corresponding POD coefficient showed a peak at $St = 0.33$. Carlsson et al. [15], who conducted LES of turbulent flow through a 90° bend at $Re = 34,000$, also observed a single swirl pattern as the first POD mode with a high-frequency ($St \approx 0.5 - 0.6$) oscillation. More recently, Hufnagel et al. [16] studied swirl switching in a 90° bend at $Re = 11,700$ via direct numerical simulation (DNS) and performed three-dimensional POD, showing modal oscillations at $St = 0.16 \text{ and } 0.32$.

Some researchers believe the origin of swirl switching to be large-scale structures coming from the straight section upstream of the bend. Sakakibara and Machida [17] measured the velocity distribution of turbulent flow upstream and downstream of a 90° bend using PIV and analyzed the stagnation point moving azimuthally in the pipe cross section downstream, characterizing the alternating domination of one of the Dean vortices. They suggested that the streaks appearing prior to the Dean vortices cause the displacement of the stagnation point, and that the estimated streaks are possibly connected to very large-scale motion (VLSM). This idea was also supported by Hellström et al. [14] and Kalpakli Vester et al. [18].

However, Noorani and Schlatter [19] argued in their DNS work that swirl switching was due to the curvature itself, because this was found in toroidal pipes with no straight section. Whereas Carlsson et al. [15] concluded that low-frequency ($St \leq 0.01$ and $St \approx 0.13$) switching was a consequence of VLSM, they also found high-frequency ($St \approx 0.5 - 0.6$) modes originating in the bend. To our knowledge, the latest result is that of Hufnagel et al. [16], who observed that the wave-like structure originating in the bend traveled in the streamwise direction, leading to switching in the pipe cross section.

An experimental study by Kalpakli et al. [20] is one of a few on turbulent bend flow with pulsation close to that in an engine. In this work, stereo PIV was used to measure the velocity distribution downstream of a 90° bend for $Re \approx 24,000$ and a Womersley number of $\alpha = 41 \text{ and } 71$ [$\alpha = (D/2)(\omega/\nu)^{0.5}$, where ω is the angular frequency of pulsation]. The result for pulsatile flow was formation of Dean vortices during one cycle. Although they applied POD to velocity data of the pulsatile flow, the analysis was just filtering, and there was no description of

unsteady structures with time scales much shorter than that of the pulsation, such as swirl switching.

In a previous study [21], we dealt with pulsatile turbulent flow through an S-shaped double-bend duct at $Re = 48,000$ and $\alpha = 70.9$. The main result was that flow reversal, also viewed as flow separation, appeared on the inner wall during flow deceleration, as often occurs with unsteady laminar flow through a bend [22, 23, 24]. We also presented secondary flow structures in terms of phase-averaged fields, but did not describe transient features of the secondary flow because of the limited sampling rate of the stereo PIV system.

It remains to be seen how secondary motion behaves unsteadily in pulsatile turbulent flow through a bend. The objective of this study is to extend understanding of fluid dynamical phenomena to unsteady flow structures, which are encountered in intake/exhaust flow of internal combustion engines. We investigate pulsatile turbulent flow through an S-shaped double-bend duct, which is often used in engine manifolds, via time-resolved stereo PIV. The PIV measurements are performed with high temporal resolution by using high-speed cameras to capture the unsteady behavior of large-scale secondary motion such as swirl switching. POD of the obtained velocity data is discussed in view of the literature, and the modes and time coefficients are compared between steady and pulsatile cases.

2 Experimental setup

The experiments were conducted with a flow rig capable of providing both steady and pulsatile flows. The rig is illustrated in Fig. 1. A blower (Showa Denki, EM-H22) supplied room-temperature (approximately 297 K) air to a circularly sectioned pipe. Pulsatile flow was generated in a way similar to that in the studies by Benjamin et al. [25] and Hirata et al. [26], by rotating a disk in which four vent holes were arranged at even intervals circumferentially. An inverter-controlled AC motor rotated the disk at a constant speed, and thus the pipe cross section was opened/closed periodically. Steady flow was realized by keeping the disk at the position where the cross section was entirely open. The created pulsatile or steady flow was delivered into a test section through a straight pipe.

The test section was made of transparent acrylic to enable optical access. The difference in refractive index between acrylic and the working fluid (air) would cause image distortion when photographing through a curved surface during PIV measurement. To reduce the distortion, a square was used as the cross-sectional shape. In a squarely sectioned straight duct, turbulent flow coexists with secondary vortices in the duct corner owing to Reynolds stress imbalance, which is secondary flow of Prandtl's second kind. However, the effect of this weak secondary motion is overwhelmed by pressure-driven secondary flow in a bend [27]. In our study, we consider curvature-induced secondary flow of Prandtl's first kind to be dominant, and our secondary flow is similar to that in a circularly sectioned pipe. In fact, our previous studies [21, 28] on a squarely

sectioned bend duct presented Dean- and Lyne-type flows as found in a circularly sectioned bend pipe.

The test section had two 90° bends each with a hydraulic diameter of D = 32 mm and curvature radius of R = 48 mm. Hereafter, we refer to the upstream and downstream bends as the first bend and second bend, respectively. Both bends were connected by a 5D-long straight duct. Straight ducts of length 25D were attached to the inlet of the first bend and the outlet of the second bend. To prevent the flow distorted by the rotating disk from flowing into the test section, a 6D-long honeycomb was inserted at the circularly sectioned pipe just before the 25D straight duct. The time waveform of the pulsatile bulk velocity (and pressure) depends strongly on the entire duct length. We determined the length of the straight duct such that the bulk velocity showed a waveform as sinusoidal as possible to simplify the effect of flow acceleration and deceleration on unsteady flow structures. Although the 25D length of the upstream duct might not be enough to develop the turbulent flow fully, the uniformity of the axial velocity distribution was confirmed in the straight section preceding the first bend by stereo PIV measurement before the main experiments. Figure 2 shows the time-averaged axial velocity distribution 3D upstream of the first bend entrance. The measurement method is the same as in the main experiments described below. In the straight section, the measured in-plane velocity is too small and thus not shown in the figure. The axial velocity distribution seems to be point-symmetric for both the steady case and the pulsatile case in which the rotating disk effect occurs.

The velocity fields 1D downstream of the first and second bends were measured for both the steady and pulsatile cases using time-resolved stereo PIV. The flow was seeded with olive oil atomized by a Laskin nozzle-based mist generator (Flowtech Research). The resulting seeding particles were injected into the upstream pipe preceding the test section in two different directions to seed the flow homogeneously.

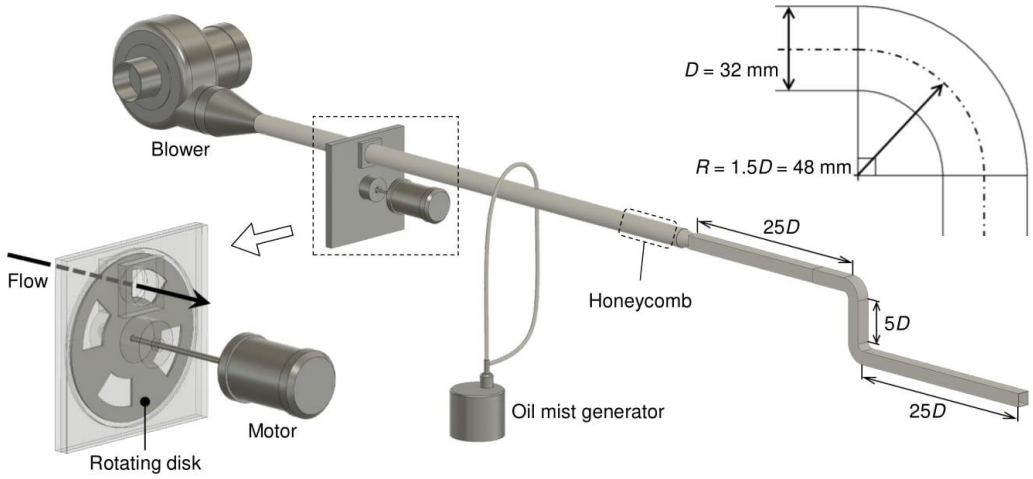

Fig. 1 Schematic of the flow rig used for PIV measurements. The pulsation generator is shown at the bottom left. The bend shape is shown at the top right with the geometrical parameters: duct diameter D and curvature radius R

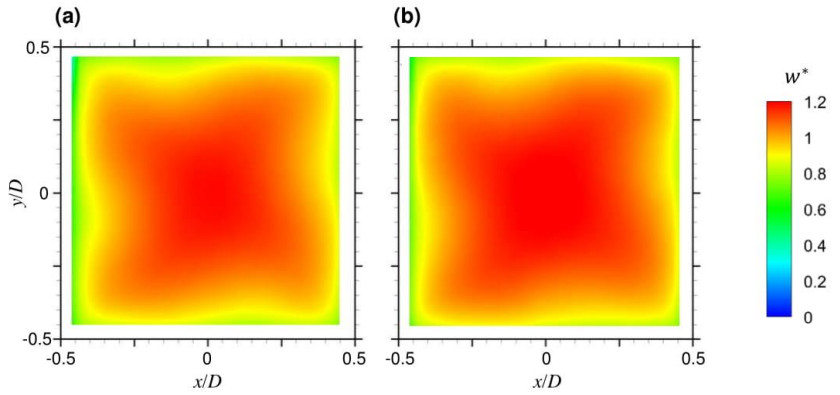

Fig. 2 Time-averaged axial velocity distribution 3*D* upstream of the first bend entrance for **a)** the steady case and **b)** the pulsatile case. The data were obtained in the preliminary PIV measurement. The contours indicate the normalized axial velocity $w^* = w/\overline{w_b}$, where w is the axial velocity and $\overline{w_b}$ is the time-averaged bulk velocity.

Figure 3 is the experimental configuration of the PIV measurement at 1*D* downstream of the first bend. The PIV system consisted of a light source, two cameras, and a delay pulse generator (Flowtech Research, FtrVSD2000) (not shown in Fig. 3). The seeded flow was illuminated by an Nd:YAG double-pulsed laser (Continuum, Mesa PIV, 9 mJ/pulse at 5 kHz, 532-nm wavelength). A 2-mm-thick light sheet was produced by passing the laser beam through a cylindrical lens. The scattered light from seeding particles was photographed by high-speed CMOS cameras (Photron, FASTCAM SA-Z, 1024 × 1024 pixels at 10,000 fps) that were aligned at approximately 45° to the normal of the light-sheet plane. Nikon lenses with 105-mm focal length were mounted and inclined on the cameras to satisfy the Scheimpflug condition [29]. The magnification factor was approximately 0.04 mm/pixel. To calibrate the cameras, images of an in-house calibration target were taken in the plane of the light sheet, as in studies such as Soloff et al. [30]. A sixth-order polynomial fit was used as the mapping function of each camera.

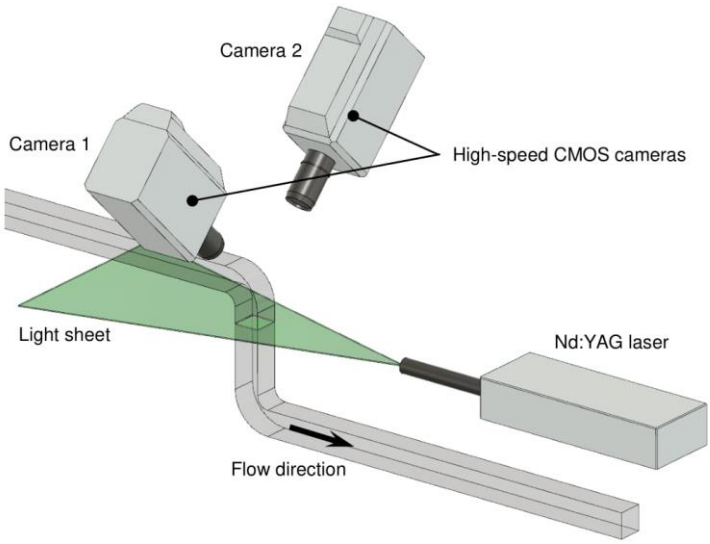

Fig. 3 Arrangement of the test section and PIV equipment consisting of a laser and cameras

The laser and cameras were synchronized through the delay pulse generator, and the PIV system was operated with frame straddling. The sampling rate of the PIV measurements was 5 kHz, equivalent to $St = 8.67$ (based on the hydraulic diameter and time-averaged bulk velocity calculated from the PIV data). Our literature survey found that the Strouhal number, which is associated with the oscillating secondary motion in steady turbulent flow through a bend, is on the order of 10^{-1} at most. Therefore, we considered our measurement sampling rate to be high enough. We took 5,000 image pairs resulting in a one-second measurement duration for each case.

The time interval between laser pulses was determined so that the out-of-plane displacement of the particles was less than one quarter of the light-sheet thickness [31]. To reflect the time interval accurately in calculating velocities, the light-emitting interval was confirmed using a biased photodetector (Thorlabs, DET10A/M). The measured time interval was 20.1 μs for all cases.

The software FtrPIV (Flowtech Research) was used for PIV post-processing. The first procedure was to subtract the background image from the particle images. The grids for vector calculation were specified inside the area of a square of dimensions 30 mm × 30 mm, in which the calibration target was placed during the camera calibration. The grid spacing (vector spacing) was 22 pixels, corresponding to 0.860 mm in actual size. The image pairs were correlated using a direct cross-correlation algorithm with an interrogation window of 45 × 45 pixels. Figure 4 shows the probability densities of the particle displacements obtained from the preliminary analysis in which a square search area of 75 × 75 pixels was arranged to search for a correlation peak within ±15 pixels in both the horizontal and vertical directions. The overall particle displacement in the images was downstream over time in this experimental configuration. As a result, the detected displacements were within ±5 pixels in the horizontal direction and from −15 pixels to 2 pixels in the vertical direction. Accordingly, we used a rectangular search area of 62 × 55 pixels (Fig. 5) for all locations and cases. In this way, we did not identify vectors that seemed to be spurious without an algorithm for removing such vectors owing to the necessary minimum size of the search area.

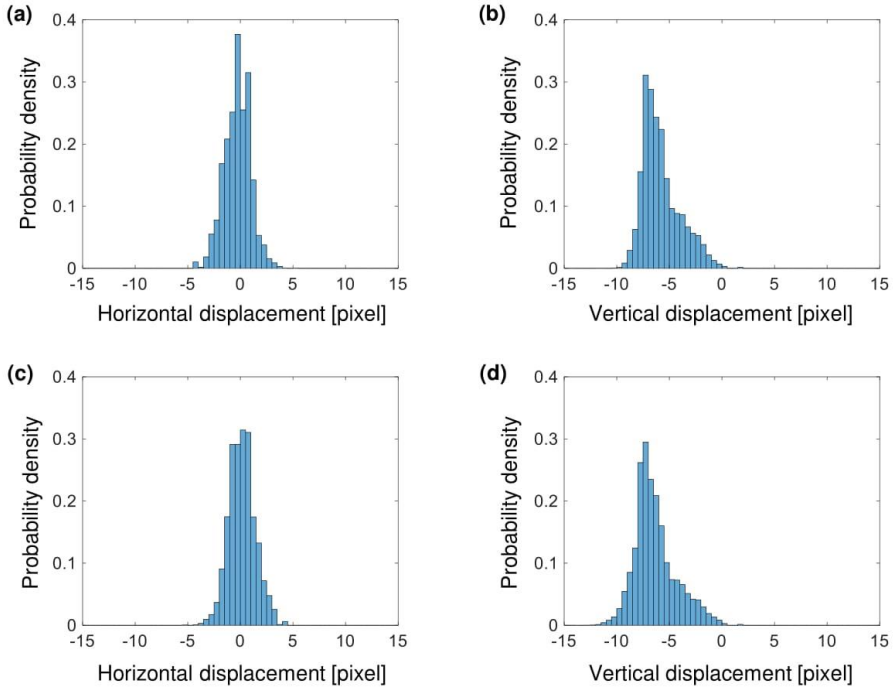

Fig. 4 Probability densities of the particle displacements obtained from the first 200 image pairs, which were taken at the first bend for the pulsatile case. **a)** Camera 1, horizontal displacement; **b)** camera 1, vertical displacement; **c)** camera 2, horizontal displacement; **d)** camera 2, vertical displacement

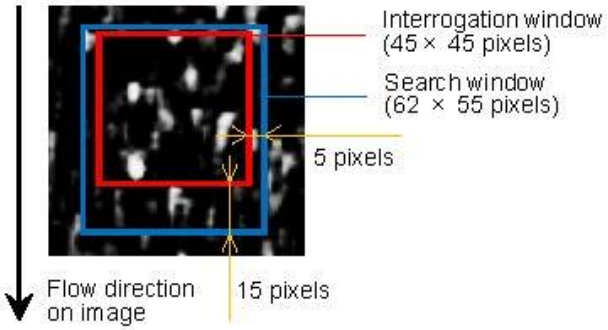

Fig. 5 Definition of an interrogation window and search window for PIV post-processing. Each window is indicated by red and blue lines on a particle image

Figure 6 shows the definition of object coordinates in the first bend (x_1, y_1, z_1) and second bend (x_2, y_2, z_2), where x_1 and x_2 are normal to the plane of symmetry, y_1 is outward of the first bend while y_2 is inward of the second bend, and z_1 and z_2 are normal to the planes of the light sheet (the cross-sectional planes). The origin of each coordinate is at the center of the duct cross section. Hereafter, the three corresponding velocity components are denoted by (u, v, w).

Figure 7 shows the waveform of the instantaneous bulk velocity at the cross section 1D downstream of the first bend for the steady and pulsatile cases. The data were obtained from the axial velocity component w measured with PIV. The graph is presented for one rotation of the disk, and thus four clear peaks are seen in the pulsatile waveform. The steady case was determined

such that the time-averaged bulk velocity was as close to that of the pulsatile cases as possible. The Reynolds numbers based on the time-averaged bulk velocity were $Re = 36,700$ for the steady case and $Re = 37,800$ for the pulsatile case. The pulsation frequency was 34 Hz, corresponding to a Womersley number of $\alpha = 59.1$. This pulsatile condition is equivalent to 1,020 rpm in a four-cylinder engine.

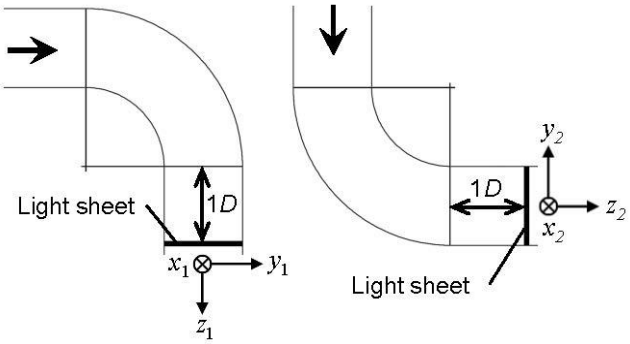

Fig. 6 Definition of coordinate system downstream of the first bend (left) and second bend (right)

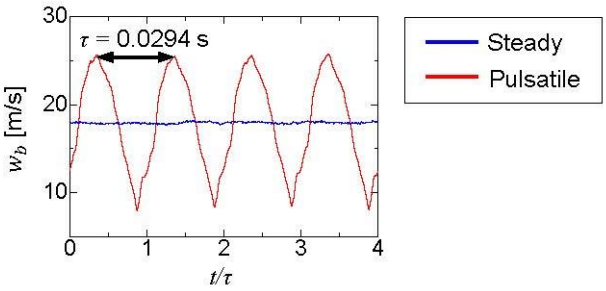

Fig. 7 Time-series bulk velocity from the PIV data downstream of the first bend for the steady and pulsatile cases. The time on the horizontal axis is normalized with the period of pulsation, τ

3 Results and discussion

3.1 Instantaneous and time-averaged fields

Figure 8 shows the instantaneous velocity fields in the cross-sectional plane 1*D* downstream of the first bend for the steady and pulsatile cases. The in-plane components (*u*, *v*) are denoted by vectors, and the axial component *w* by a colored contour. In the steady case (Fig. 8a), high-speed axial flow appears on the outer wall owing to the centrifugal force, while the slower flow is on the inner wall. Prevailing Dean motion is not seen in the instantaneous field containing turbulent fluctuations, as also described by Hellström et al. [14]. The shift of the high-speed axial flow toward the outer wall is also seen in the pulsatile case (Fig. 8b, c) and is more evident during

deceleration than during acceleration. A similar tendency was reported by Komai and Tanishita [32] and Boiron [33], who found that the maximum axial velocity, which was near the inner wall during acceleration, moved toward the outer wall during deceleration. The shift of the axial flow is due to the fact that the secondary flow would prevail at this location (1*D* downstream of the bend exit) during deceleration (see Section 3.2.2).

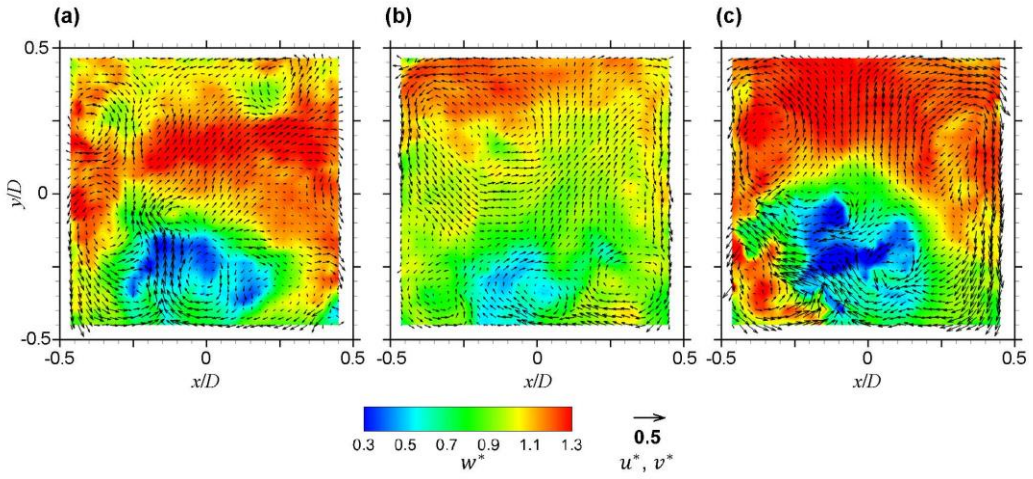

Fig. 8 Instantaneous velocity fields obtained from the PIV at the cross section downstream of the first bend **a)** for the steady case (t/τ = 0.11 in Fig. 7), **b)** during acceleration for the pulsatile case (t/τ = 0.11 in Fig. 7), and **c)** during deceleration for the pulsatile case (t/τ = 0.63 in Fig. 7). Vectors and color contours indicate the in-plane velocities $(u^*, v^*) = (u/\overline{w_b}, v/\overline{w_b})$ and axial velocity $w^* = w/\overline{w_b}$, where $\overline{w_b}$ is the time-averaged bulk velocity

To know fundamental flow structures induced by passing the flow through the double 90° bend, we computed the time-averaged fields over 5,000 successive snapshots. The time-averaged velocity fields 1*D* downstream of the first and second bends are presented in Fig. 9 in a similar manner to Fig. 8, but the vectors are plotted at half the full resolution in both the *x* and *y* directions. Downstream of the first bend (Fig. 9a, b), the in-plane flow is in the centrifugal force direction (toward the outer wall) over a wide region of the cross section, while the flows close to the left and right side walls are in the radial pressure gradient direction (toward the inner wall), resulting in Dean motion, for both the steady and pulsatile cases. That the Dean motion appears even in the pulsatile turbulent case agrees with the results of Kalpakli et al. [20] and our previous studies [21, 28]. The axial velocity distribution is distorted in accordance with the Dean motion. Downstream of the second bend (Fig. 9c, d), Lyne-type circulation forms in the core of the cross section for both cases. This secondary motion is not due to either the pulsation or square cross section, but to the non-uniform axial flow developed through the first bend and the straight section preceding the second bend. At the second bend, the radial pressure gradient is dominant over the centrifugal force in the core of the cross section. The reader is referred to our previous study [28] for more details on formation of Lyne-type vortices. The axial velocity distribution downstream of the second bend is not as distorted as in the first bend, owing to the weak centrifugal force. The

time-averaged structures do not make much difference between the steady and pulsatile cases as a whole.

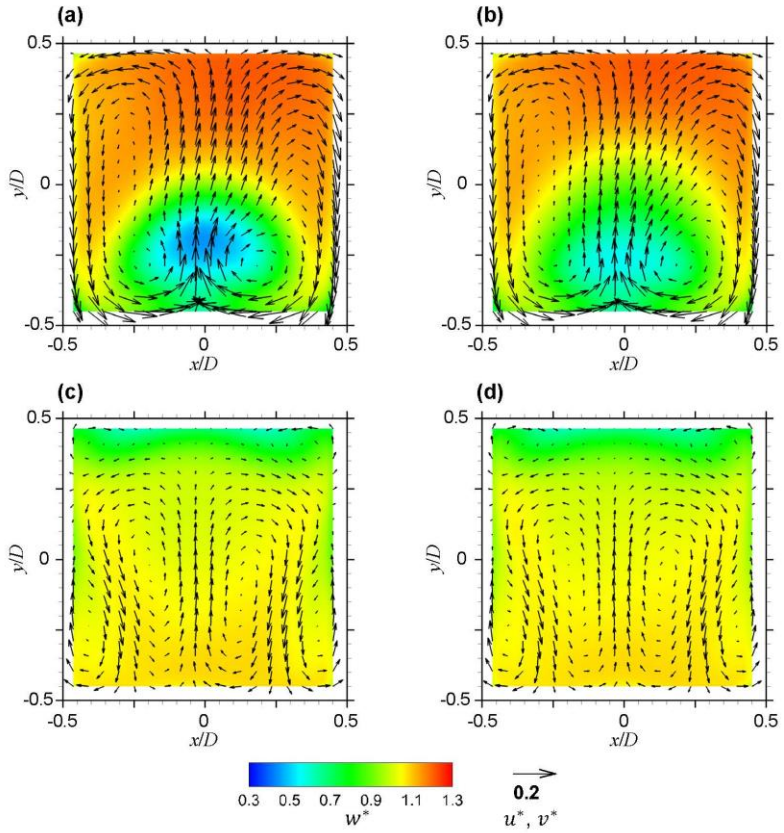

Fig. 9 Time-averaged velocity fields from the PIV data. **a)** First bend, steady case; **b)** first bend, pulsatile case; **c)** second bend, steady case; **d)** second bend, pulsatile case. Vectors are plotted at half the full resolution in both the *x* and *y* directions

3.2 Proper orthogonal decomposition

We applied POD only to the in-plane velocity components (*u*, *v*) in the two-dimensional domain, as in Hellström et al. [14], to eliminate the effects of the velocity pulsation in the axial direction and any streamwise structures.

Extracting coherent structures via POD lies in finding the deterministic function ϕ that maximizes the mean-square projection onto the time-dependent flow fields [34]. This maximization results in the following integral eigenvalue problem of the Fredholm type:

$$\int C_{ij}(X;X')\phi_j^{(n)}(X')dX' = \lambda^{(n)}\phi_i^{(n)}(X)\,. \qquad (1)$$

Here, X denotes the space variable [(x_1, y_1) or (x_2, y_2) in this analysis], and $C_{ij}(X;X')$ is the time-averaged two-point correlation function, defined by:

$$C_{ij}(X;X') = \overline{u_i(X,t)u_j(X',t)} \quad , \qquad (2)$$

where $u_i(X,t)$ is the *i*-th component of the velocity vector [$(u_1,u_2) = (u,v)$ in this analysis] at time *t*. In Eq. (1), the eigenfunctions $\phi^{(n)}$ represent the spatial POD modes ordered according to the size of the corresponding eigenvalues $\lambda^{(n)}$ (*n* indicates the mode number). We denote the most energetic structure as mode 0 ($\phi^{(0)}$). The POD time coefficients can be recovered by projecting the instantaneous fields onto the POD modes and are given by the equation

$$a^{(n)}(t) = \int u_i(X,t)\phi_i^{(n)}(X)dX \ . \qquad (3)$$

The POD was performed as the eigenvalue problem for the velocity correlation matrix. When calculating the velocity correlation matrix on the basis of Eq. (2), we used 5,000 successive snapshots, giving convergence of both the eigenvalues and eigenvectors [35].

3.2.1 Modes

Figure 10 shows the first three POD modes 1*D* downstream of the first bend for each flow case. The modes are illustrated by contour lines of the in-plane stream function, representing streamlines of the in-plane velocity, to visualize organized structures clearly. First, the modes for the steady case are focused. The Dean vortices are characterized as mode 0. Mode 1, representing the first fluctuating structure, consists of a single swirl spanning the whole cross section, as also observed in turbulent flow through a circularly sectioned bend [13, 14, 15, 16, 18, 20], and this structure is associated with swirl switching. Because the time average of the corresponding POD coefficient is zero (not shown in the figure), the swirling motion does not contribute to the mean field [36], as seen in the time-averaged field of the Dean motion (Fig. 9a). The structure of mode 2 consists of two vortices and is similar to a double swirl [16] and to tilted Dean vortices [14, 18, 19]. The modes for the turbulent flow through the squarely sectioned bend duct agree with those in the literature for circularly sectioned bend pipes. This implies that the energetic structures observed here are associated not with Reynolds-stress-driven secondary flow specific to the square section but rather curvature-driven secondary flow similar to circular-pipe flow.

As for pulsating flow downstream of the first bend, the first three modes contain clear vortices, unlike the POD of the pulsatile flow data of Kalpakli et al. [20], and represent the Dean vortices and the single and double swirls. These flow patterns are very similar to those of the steady case. A noteworthy result is that the in-plane coherent structures extracted by the POD are not subject to the pulsation.

Figure 11 shows the in-plane flow reconstructed with the first two modes, containing 55.2% of the total energy, at two representative times for the pulsatile case. The reconstruction clearly shows that the flow switches between two states with one Dean vortex dominating the other, which is swirl switching. To our knowledge, this study is the first to identify swirl switching in pulsatile flow.

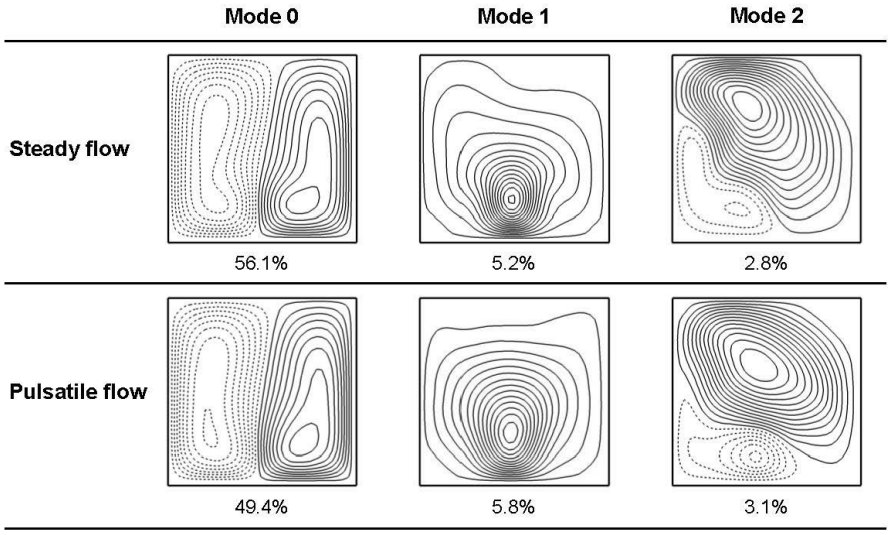

Fig. 10 POD modes 0, 1, and 2 (from left to right) downstream of the first bend for the steady case (top row) and pulsatile case (bottom row). The in-plane flow structures are indicated as contour lines of the stream function, representing streamlines. Solid and dashed lines denote clockwise and anticlockwise vortices, respectively. The percentage below each mode is the proportion of kinetic energy to total energy ($\lambda^{(n)}/\Sigma\lambda^{(n)}$)

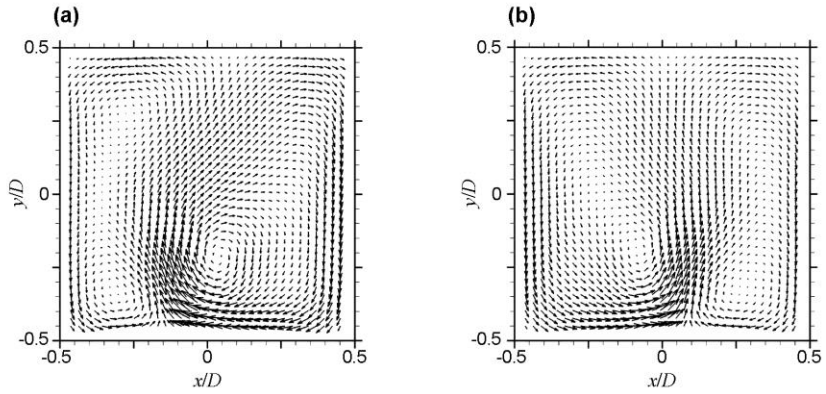

Fig. 11 In-plane flow fields reconstructed using the first two POD modes downstream of the first bend for the pulsatile case at two representative times, **a)** $t/\tau = 0.66$ and **b)** $t/\tau = 0.76$ in Fig. 7

Figure 12 is similar to Fig. 10 but for the second bend. For each of the steady and pulsatile cases, the structure of mode 0 is naturally close to the time-averaged field (Fig. 9). The Lyne-type vortices are evident in mode 0 and are surrounded by the other vortices. A swirling flow spanning the cross section is captured as mode 1, but two additional vortices are present, unlike the case of the first bend (Fig. 10). Mode 2 consists of two counter-rotating vortices with one of them splitting into two parts. There is a visible difference in the number of vortices between the first and second bends for all presented modes. As stated in Sec. 3.1, the non-uniform axial flow before the second bend affects secondary flow formation in the second bend, resulting in additional vortices in the time-averaged field (Fig. 9). This effect is apparent even in the POD modes of vortices other than

those in the first bend. As in the first bend, the flow reconstruction (not shown here) reveals the alternating domination of all vortices in mode 0: switching occurs even in the second bend.

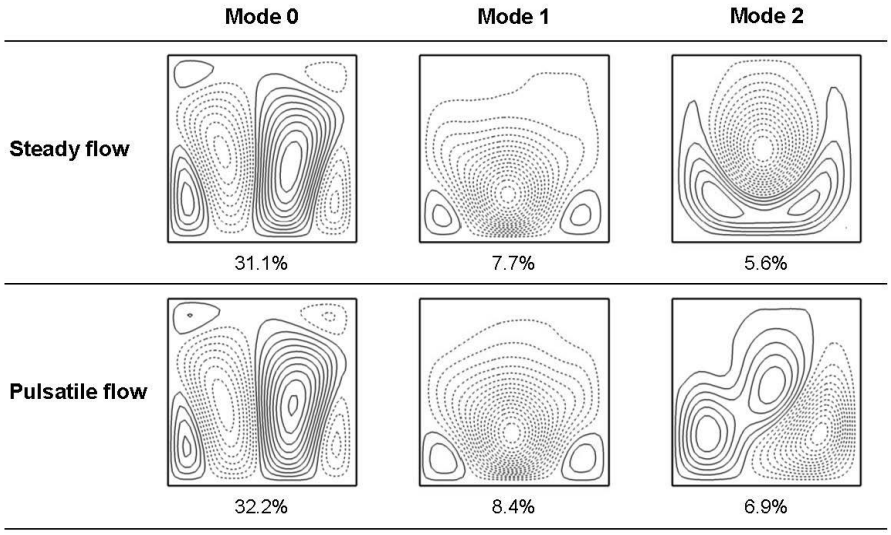

Fig. 12 POD modes 0, 1, and 2 (from left to right) downstream of the second bend for the steady case (top row) and pulsatile case (bottom row). The in-plane flow structures are indicated as contour lines of the stream function, representing streamlines. Solid and dashed lines denote clockwise and anticlockwise vortices, respectively. The percentage below each mode is the proportion of kinetic energy to total energy ($\lambda^{(n)}/\Sigma\lambda^{(n)}$).

3.2.2 Temporal behavior of the modes

In this section, the unsteadiness of the energetic structure is discussed in terms of the POD time coefficient, which indicates when the corresponding mode is active. We examine the POD time coefficient for modes 0 and 1 showing the Dean motion and single swirl, respectively, that contribute most to the swirl switching. We focus on the data collected only at the first bend because the main difference is in the vortices (Figs. 10 and 12), without much change in the temporal behavior of the switching between the two bends.

The graph in Fig. 13 shows the time coefficients of the first two modes and the bulk velocity waveform for the pulsatile case. The coefficients are motion-averaged with a cut-off frequency of 450 Hz, corresponding to $St = 0.78$, to remove short time-scale fluctuations due to background turbulence. The time coefficient of mode 0 (Dean motion) seems to follow the temporal change in the bulk velocity. To quantitatively evaluate the correlation between the mode 0 time coefficient and the bulk velocity, we computed the cross-correlation function given by:

$$R(w_b; a^{(0)}, \Delta t) = \frac{\sum_i \left\{ w_b(t_i) - \overline{w_b} \right\} \left\{ a^{(0)}(t_i + \Delta t) - \overline{a^{(0)}} \right\}}{\sqrt{\sum_i \left\{ w_b(t_i) - \overline{w_b} \right\}^2 \sum_i \left\{ a^{(0)}(t_i + \Delta t) - \overline{a^{(0)}} \right\}^2}}, \quad (4)$$

where Δt is the time lag. The graph of this function (Fig. 14) shows a clear correlation between the two signals. The high-speed axial flow likely induces the strong secondary flow, which would lead to large amplitude of mode 0 at the peak bulk velocity. However, there is a positive time lag for $\Delta t/\tau = 0.11$: a peak in the time coefficient of mode 0 appears during deceleration. We assume this time lag occurs because the measurement plane is located downstream of the bend section where the secondary flow arises. The time lag can also be estimated from the time period in which the curvature-induced secondary flow is transported to the measurement plane ($1D$ downstream of the bend exit). We treat the distance from the bend to the measurement plane as being $L \approx R \cdot (\pi/4) + 1D \approx 70$ mm (from the midsection of the bend to the measurement plane on the center line of the duct), and approximate the transportation velocity of secondary flow as the time-averaged bulk velocity $\overline{w_b} \approx 18$ m/s. Thus, the time lag is $\Delta t \approx L/\overline{w_b} = 0.13\tau$, which is close to the value obtained from the above cross-correlation function. That the Dean motion is more evident during deceleration agrees with the pulsatile turbulent flow data of Kalpakli et al. [20], who also measured downstream of the bend exit and found Dean-type vortices forming during deceleration even though no vortices were present at the start of deceleration (the end of acceleration). The strong Dean motion during deceleration causes the aforementioned shift of the high-speed axial flow at this time (Fig. 8c). The time coefficient of mode 1 (swirl switching) fluctuates with higher frequency than the axial pulsation, suggesting that domination of each vortex alternates several times during one pulsation.

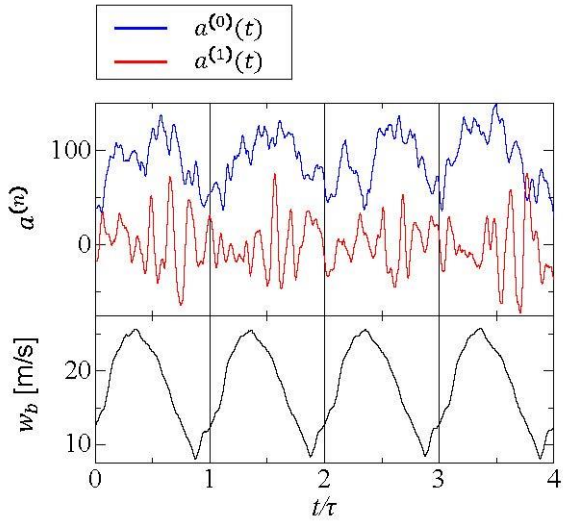

Fig. 13 POD time coefficients of modes 0 and 1 downstream of the first bend for the pulsatile case. The waveform of the bulk velocity w_b is also shown below the graph of the coefficients

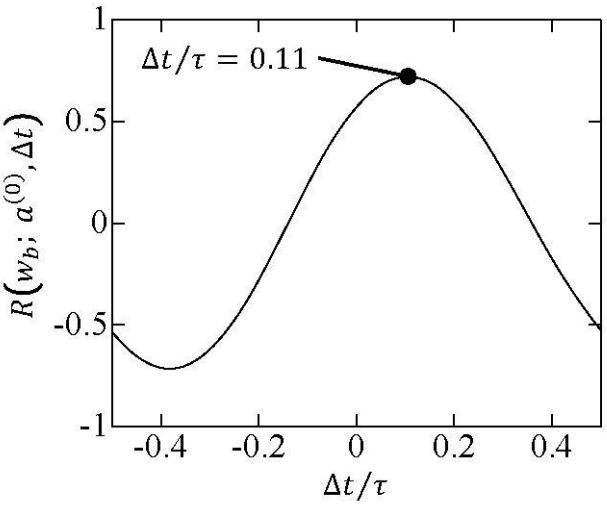

Fig. 14 Cross-correlation function of the bulk velocity and the POD time coefficient of mode 0

Previous studies [13, 14, 15, 16, 18, 19] analyzed POD time coefficients in the frequency domain to determine the frequency response of swirl switching. In this paper we have introduced time-frequency analysis to study the relation between switching and pulsation.

The time-frequency energy distribution of the time coefficient of mode 1 (swirl switching) was obtained with the continuous Morlet wavelet transformation [37], and is presented in Fig. 15 for the steady and pulsatile cases. This figure also shows the Fourier spectrum of the mode 1 coefficient, which was calculated with Welch's method [38], and the time coefficient of mode 0 (Dean motion), allowing us to track the switching frequency while the intensity of mode 0 changes. The Fourier spectrum for each case has a peak at $St \approx 0.3$ (corresponding to $f \approx 173$ Hz), about the same as those found by Hellström et al. [14] and Hufnagel et al. [16], whose spectra peak at $St = 0.33 \text{ and } 0.32$, respectively, for the time coefficient of mode 1 for the single swirl. Because the Fourier spectra for the steady and pulsatile cases have similar patterns, there is little difference in time-averaged switching between them. The wavelet spectra also peak at $St \approx 0.3 - 0.4$ for both flows. (Note that in the wavelet spectra the maximum contour level was set to display a wide range of the wavelet coefficient, and therefore the brightness, representing power, is saturated at this frequency). For the steady case, the wavelet power is randomly distributed in the time direction. However, for the pulsatile case, the wavelet power is strongly correlated with the time coefficient of mode 0: the wavelet power increases with an increase in the mode 0 time coefficient. Given that the mode 0 time coefficient follows the bulk velocity waveform (Figs. 13 and 14), the significance of the mode 1 structure, which is associated with the wavelet power, increases intermittently following the pulsatile bulk velocity. More specifically, the swirling motion becomes energetic when the axial flow decelerates.

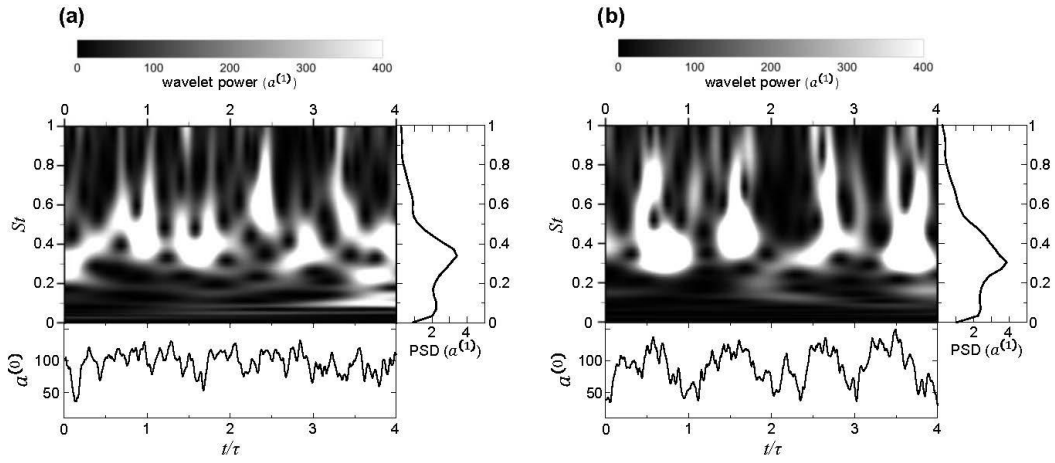

Fig. 15 Wavelet spectra of the mode 1 time coefficient ($a^{(1)}$) downstream of the first bend for **a)** the steady case and **b)** the pulsatile case. The power spectral density (PSD) of $a^{(1)}$ is also shown on the right side of each wavelet spectrum. The time series waveform presented below the wavelet spectrum is the mode 0 time coefficient ($a^{(0)}$)

4 Conclusion

Both steady and pulsatile flows in an S-shaped duct comprising two 90° bends were investigated using time-resolved stereo PIV. The measurements were conducted in the cross sections at one pipe diameter downstream of the bend exits. Our experiments yield the time-dependent velocity fields, which help to compensate for lack of information on pulsatile turbulent flow.

POD was used to isolate the energetic structures from the velocity data set. The steady case manifests Dean motion and a single swirl downstream of the first bend as modes 0 and 1, respectively, as often reported by studies on turbulent flow through a circularly sectioned 90° bend pipe. The secondary flow downstream of the second bend consists of multiple vortices in the time-averaged fields due to the first bend, as also reported in our previous studies [21, 28]. This is seen even in modes 1 and 2 as well as mode 0, representing the mean field. A noteworthy result in this study is that swirl switching occurs in pulsatile flow, which is a new finding as far as we know.

The time-averaged fields and POD modes show no clear differences between the steady and pulsatile cases. However, POD time coefficients reveal unsteady behavior unique to pulsatile flow. Our Fourier spectra of the time coefficient of the single swirl show a peak at about the same point as in previous studies, for both the steady and pulsatile cases. In addition, we used a wavelet transformation to obtain the time-frequency representation of the time coefficient, finding that the switching frequency in pulsatile flow prevails more as the intensity of mode 0 (the Dean motion) increases. The energies of both the Dean motion and single swirl increase temporally during deceleration, because the measurement location is in the straight section downstream of the bend.

Acknowledgments

This work was partially supported by a research grant from The Hiroshima University Education and Research Support Foundation. Mark Kurban, M. Sc., from Edanz Group (www.edanzediting.com/ac) edited a draft of this manuscript.

Compliance with Ethical Standards

Conflict of interest: The authors declare that they have no conflict of interest.

References

1. Merati, P., Mirhashemi, A., Fajardo-Hansford, C., Liu, T.: Flow measurements in the exhaust system of a motorized engine. Int. J. Automot Technol. 18(4), 563-569 (2017)
2. Xu, J.: Flow analysis of engine intake manifold based on computational fluid dynamics. J. Phys. Conf Ser. 916, 012043 (2017)
3. Dean, W.R.,: XVI. Note on the motion of fluid in a curved pipe. Philos. Mag. 4(20), 208-223 (1927)
4. Dean, W.R.: LXXII. The stream-line motion of fluid in a curved pipe (Second paper). Philos. Mag. 5(30), 673-695 (1928)
5. Lyne, W.: Unsteady viscous flow in a curved pipe. J. Fluid Mech. 45(1), 13-31 (1971)
6. Chang, L., Tarbell, J.: Numerical simulation of fully developed sinusoidal and pulsatile (physiological) flow in curved tubes. J. Fluid Mech. 161, 175-198 (1985)
7. Sudo, K., Sumida, M., Yamane, R.: Secondary motion of fully developed oscillatory flow in a curved pipe. J. Fluid Mech. 237, 189-208 (1992)
8. van Wyk, S., Prahl Wittberg, L., Bulusu, K.V., Fuchs, L., Plesniak, M.W.: Non-Newtonian perspectives on pulsatile blood-analog flows in a 180° curved artery model. Phys. Fluids. 27, 071901 (2015)
9. Najjari, M.R., Plesniak, M.W.: Evolution of vortical structures in a curved artery model with non-Newtonian blood-analog fluid under pulsatile inflow conditions. Exp. Fluids. 57, 100 (2016).
10. Tunstall, M., Harvey, J.: On the effect of a sharp bend in a fully developed turbulent pipe-flow. J. Fluid Mech. 34(3), 595-608 (1968)
11. Brücker, C.H.: A time-recording DPIV-study of the swirl-switching effect in a 90° bend flow. In: Proc. 8th Int Symp Flow Vis. Sorrento (NA), Italy, September 1-4, pp 171.1-171.6 (1998)
12. Rütten, F., Schröder, W., Meinke, M.: Large-eddy simulation of low frequency oscillations of the Dean vortices in turbulent pipe bend flows. Phys. Fluids. 17, 035107 (2005)

13. Sakakibara, J., Sonobe, R., Goto, H., Tezuka, H., Tada, H., Tezuka, K.: Stereo-PIV study of turbulent flow downstream of a bend in a round pipe. In: Proc. 14th Int Symp Flow Vis. EXCO Daegu, Korea, June 21-24 (2010)
14. Hellström, L., Zlatinov, M., Cao, G., Smits, A.: Turbulent pipe flow downstream of a 90° bend. J. Fluid Mech. 735, R7 (2013)
15. Carlsson, C., Alenius, E., Fuchs, L.: Swirl switching in turbulent flow through 90° pipe bends. Phys. Fluids. 27, 085112 (2015)
16. Hufnagel, L., Canton, J., Örlü, R., Marin, O., Merzari, E., Schlatter, P.: The three-dimensional structure of swirl-switching in bent pipe flow. J. Fluid Mech. 835, 86-101 (2018)
17. Sakakibara, J., Machida, N.: Measurement of turbulent flow upstream and downstream of a circular pipe bend. Phys. Fluids. 24, 041702 (2012)
18. Kalpakli Vester, A., Örlü, R., Alfredsson, P.H.: POD analysis of the turbulent flow downstream a mild and sharp bend. Exp. Fluids. 56, 57 (2015)
19. Noorani, A., Schlatter, P.: Swirl-switching phenomenon in turbulent flow through toroidal pipes. Int. J. Heat Fluid Flow. 61(A), 108-116 (2016)
20. Kalpakli, A., Örlü, R., Alfredsson, P.H.: Vortical patterns in turbulent flow downstream a 90° curved pipe at high Womersley numbers. Int. J. Heat Fluid Flow. 44, 692-699 (2013)
21. Oki, J., Kuga, Y., Ogata, Y., Nishida, K., Yamamoto, R., Nakamura, K., Yanagida, H., Yokohata, H.: Stereo and time-resolved PIV for measuring pulsatile exhaust flow from a motorized engine. J. Fluid Sci Tech. 13,1 (2018)
22. Chandran, K., Yearwood, T.: Experimental study of physiological pulsatile flow in a curved tube. J. Fluid Mech. 111, 59-85 (1981)
23. Talbot, L., Gong, K.: Pulsatile entrance flow in a curved pipe. J. Fluid Mech. 127, 1-25 (1983)
24. Timité, B., Castelain, C., Peerhossaini, H.: Pulsatile viscous flow in a curved pipe: Effects of pulsation on the development of secondary flow. Int. J. Heat Fluid Flow. 31(5), 879-896 (2010)
25. Benjamin, S., Roberts, C., Wollin, J.: A study of pulsating flow in automotive catalyst systems. Exp. Fluids. 33(5), 629-639 (2002)
26. Hirata, K., Kubo, T., Hatanaka, Y., Matsushita, M., Shobu, K., Funaki, J.: An Experimental Study of Amplitude and Frequency Effects upon a Pulsating Jet. J. Fluid Sci Tech. 4(3), 578-589 (2009)
27. Humphrey, J., Whitelaw, J., Yee, G.: Turbulent flow in a square duct with strong curvature. J. Fluid Mech. 103, 443-463 (1981)
28. Oki, J., Ikeguchi, M., Ogata, Y., Nishida, K., Yamamoto, R., Nakamura, K., Yanagida, H., Yokohata, H.: Experimental and numerical investigation of a pulsatile flow field in an S-shaped exhaust pipe of an automotive engine. J. Fluid Sci Tech. 12, 2 (2017)
29. Prasad, A., Jensen, K.: Scheimpflug stereocamera for particle image velocimetry in liquid flows. Appl. Opt. 34(30), 7092-7099 (1995)
30. Soloff, S.M., Adrian, R.J., Liu, Z.-C.: Distortion compensation for generalized stereoscopic particle image velocimetry. Meas. Sci. Technol. 8(12), 1441-1454 (1997)

31. Keane, R.D., Adrian, R.J.: Optimization of particle image velocimeters: II. Multiple pulsed systems. Meas. Sci. Technol. 2(10), 963-974 (1991)
32. Komai, Y., Tanishita, K.: Fully developed intermittent flow in a curved tube. J. Fluid Mech. 347, 263-287 (1997)
33. Boiron, O., Deplano, V., Pelissier, R.: Experimental and numerical studies on the starting effect on the secondary flow in a bend. J. Fluid Mech. 574, 109-129 (2007)
34. Lumley, J.L.: The structure of inhomogeneous turbulent flows. In: Yaglom AM, Tatarski VI (eds) Atmospheric turbulence and wave propagation. Nauka, Moscow, 166–178 (1967)
35. Semeraro, O., Bellani, G., Lundell, F.: Analysis of time-resolved PIV measurements of a confined turbulent jet using POD and Koopman modes. Exp. Fluids. 53, 1203-1220 (2012)
36. Hellström, L.H.O., Zlatinov, M.B., Smits, A.J., Cao, G.: Turbulent pipe flow through a 90 bend. In: Proc. 7th Int Symp on Turbulence and Shear Flow Phenomena. Ottawa, Canada, July 28-31 (2011)
37. Grossmann, A., Morlet, J.: Decomposition of Hardy functions into square integrable wavelets of constant shape. SIAM J. Math. Anal. 15(4), 723-736 (1984)
38. Welch, P.: The use of fast Fourier transform for the estimation of power spectra: A method based on time averaging over short, modified periodograms. IEEE Trans. Audio Electroacoust. 15(2), 70-73 (1967)